

The response of warm absorbers to the variations in the ionizing continuum in the active galaxy NGC 4051

DEV R. SADAULA,^{1,2,3} TIMOTHY R. KALLMAN,¹ AND SIBASISH LAHA^{1,2,3}

¹*Astrophysics Science Division, NASA Goddard Space Flight Center, Greenbelt, MD 20771, USA.*

²*Center for Space Science and Technology, University of Maryland Baltimore County, 1000 Hilltop Circle, Baltimore, MD 21250, USA.*

³*Center for Research and Exploration in Space Science and Technology, NASA/GSFC, Greenbelt, Maryland 20771, USA*

ABSTRACT

We investigate the response of warm absorbers to variations in the ionizing continuum of the Seyfert 1 galaxy NGC 4051 using time-resolved X-ray observations from the *Neutron Star Interior Composition Explorer* (NICER). In this work, we have demonstrated we can perform time-resolved spectroscopic studies of warm absorbers of about ~ 5500 s time resolution using NICER data. We have extracted 15 spectra for this source, corresponding to 15 different visits to the source, or pointings, each separated by a longer Earth occultation. By modeling the spectral variability of the warm absorber with the WARMABS analytic model, we detect significant variations in the ionization parameter that correlate with changes in the ionizing flux. A time lag of approximately 5500 seconds is observed between the flux variations and the absorber's ionization response, suggesting that the gas is out of photoionization equilibrium during these periods. Using this time lag, we estimate the lower limit of the gas density $8.91 \times 10^6 \text{ cm}^{-3}$ and constrain the location of the warm absorber to within $7.02 \times 10^{16} \text{ cm}$ (~ 0.02 parsec) from the central black hole. This study uses time-resolved spectral analysis to contribute to our understanding of the physical conditions of ionized AGN outflows, such as density and location.

Keywords: Galaxy, Seyfert, X-rays, AGN, WARMABS, Black hole, Photoionization

1. INTRODUCTION

Active Galactic Nuclei (AGN) are among the most luminous and energetic objects in the universe, powered by the accretion of matter onto supermassive black holes. A significant fraction of AGNs exhibit ionized outflows, known as warm absorbers (WAs), which are detected through absorption features by partially ionized gas in their X-ray spectra (Rozanska et al. 2005; Behar et al. 2003; Crenshaw et al. 2003; Krolik & Kriss 1995; Halpern 1984). Typical WA outflow speeds are $500 - 1000 \text{ km s}^{-1}$. Some observations reveal ultrafast outflows with much larger speeds ($0.1 - 0.3c$) (Chartas et al. 2002; Pounds et al. 2003a,b; Tombesi et al. 2010). These outflows are surprising, given the fact that we expect primarily an inflow toward the black hole to fuel the AGN. Of great interest is their potential role in the AGN feedback mechanism, which influences galaxy evolution

by regulating star formation and redistributing energy throughout the host galaxy (Elvis 2000; Crenshaw et al. 2003; Blustin et al. 2005; Rosito et al. 2021).

The WA gas is heated and ionized by the strong UV and X-ray continuum radiation originating from close to the central black hole. If it is assumed that the gas is in ionization and thermal equilibrium, then WAs are characterized by their ionization parameter ($\xi = 4\pi F/n$, where F is the incident radiation flux and n is the gas density). These quantities can be directly inferred from observed spectra by comparing models for the ionization balance and opacity of WA gas with observations. This yields parameter values: $\log(\xi) \simeq -0.5 - 3.0$; column density, $N_{\text{H}} \simeq (10^{20} - 10^{22}) \text{ cm}^{-2}$ and outflow speed, $v_{\text{out}} \simeq (500 - 2000) \text{ km s}^{-1}$ (Kaastra et al. 2002; Laha et al. 2014). These values constrain the mass flux in the outflow if the geometry of the outflow is assumed. This in turn suggests that WA outflows can carry significant amounts of mass and energy, potentially affecting the host galaxy on both small and large scales (Silk & Rees 1998; Di Matteo et al. 2005; Fabian 2012; Croton et al. 2006; Cattaneo et al. 2009). However, the origin and

acceleration of WAs are unclear. Possible driving mechanisms include rotation together with magnetic fields or thermal evaporation from a cold accretion flow. One key parameter that could help to resolve this ambiguity is the WA density. The ionization parameter and column density together do not uniquely constrain this quantity.

Time-resolved spectral analysis provides an additional powerful technique to study WAs. The characteristic timescales affecting ionization, recombination, and other atomic processes depend on fundamental atomic constants, together with the density and the ionizing flux.

Departures from ionization equilibrium can be detected by comparing observations with time-dependent models. Models which assume ionization equilibrium predict particular ratios of the strengths of the various absorption lines in the spectrum; observed spectra that do not fit these predictions are likely not in ionization equilibrium. Fits of such spectra to models that incorporate time-dependent effects, if successful, can be used to infer the key physical quantities affecting time dependence, namely the gas density and the radiation flux incident on the WA. Time-dependent models have been carried out by [García et al. \(2013\)](#); [Sadaula et al. \(2023\)](#); [Sadaula & Kallman \(2024\)](#); [Gu et al. \(2023\)](#); [Li et al. \(2023a\)](#); [Luminari et al. \(2023, 2024\)](#); [Krolik & Kriss \(1995\)](#); [Juráňová et al. \(2022\)](#). Searches for time-dependent effects and fits to observed spectra have been carried out by [Rogantini et al. \(2022\)](#) and by [Gu et al. \(2023\)](#).

In our previous work ([Sadaula et al. 2023](#); [Sadaula & Kallman 2024](#)) and work by others ([Rogantini et al. 2022](#); [Li et al. 2023b](#); [Gu et al. 2023](#); [Nicastro et al. 1999](#); [Krongold 2007](#)), we have shown the variability of the central ionizing source could potentially be a useful probe for the density diagnostic of the ionizing outflow. All this work has explored a similar method to calculate time-dependent photoionization and recombination effects. That is, the time-dependent ionization is calculated due to variations in the ionizing luminosity. Then model spectra vs time are produced for different densities and fluxes. These models are then fit to observations in order to search for the signatures of time-dependent photoionization. Such signatures, if found, can be used to constrain density and flux. This procedure is challenging owing to the fact that it requires looking at the time variability of several, or many, spectral features (i.e., lines or edges) simultaneously. In what follows, we will refer to this method as ‘time-resolved time-dependent photoionization model fitting.’.

Another way to detect time-dependent ionization is to make use of a simplified heuristic model of time-dependent photoionization. That is, if the gas is ini-

tially in photoionization equilibrium with the observed radiation field, and then if the radiation field suddenly increases or decreases to a different constant value, the ionization balance in the gas will respond. The response will resemble a changing ionization parameter, with the state of the gas accurately characterized by the initial ionization parameter prior to the change in flux and by the final ionization parameter long after the change in flux. The transition between the initial and final states will take more time than the (sudden) change in the illuminating flux from the initial to the final values. We call this response time the equilibrium time, t_{eq} and it depends on an initial equilibrium photoionization timescale t_{PI} and the recombination timescale, t_{Rec} . Thus, by measuring the change in the ionization parameter from a time series of spectra, we can set limits on t_{eq} , which is technically the time lag between the variation in the ionizing flux and the ionization state of the gas. The equilibrium time directly depends on the gas density and can be used to determine its value. This is the procedure that we adopt in this paper.

Figure 1 illustrates schematically how our procedure works. We use a time series of spectra and fit each spectrum with an equilibrium model. We then compare the fit parameters, i.e., the ionization parameter and column density, with the continuum flux in each spectrum. We do this by calculating the cross-correlation function, including a variable lag. In this way we search for a lag between the ionizing continuum and the warm absorber gas. If found, such lags most likely imply departures from ionization equilibrium. We demonstrate, with simulations, that this test will detect time dependence even though it employs equilibrium models to provide the ionization parameters for the various time bin spectra.

Our method has advantages compared with the time-dependent photoionization model fitting. That method attempts to fit the time dependence of the spectrum in detail during the time of transition between equilibrium states. Our method measures the conditions in the equilibrium states before and after a change in ionizing flux and then compares the time separation of the equilibrium states with the predictions of time-dependent photoionization. Detection and characterization of the ionization balance in equilibrium models requires fewer photons than does the full characterization of time-dependent models. Detection of time dependence in a single spectrum requires detection of two or more spectral features and then demonstrating that their ratios cannot be fitted by equilibrium models. Detection of a warm absorber in equilibrium can be as simple as detecting one edge or line feature and showing that it is stronger than can be produced by cold absorption.

Thus, our method requires fewer counts than direct detection of time dependence in each spectrum. Therefore, it can probe shorter timescales and is conceptually simpler.

In this paper we use observations from the Neutron Star Interior Composition Explorer (NICER) (Gendreau et al. 2016) to constrain the properties of the warm absorber and understand its response to changes in the ionizing flux. We concentrate on time-resolved spectral variability of the warm absorber in NGC 4051, a well-studied Narrow Line Seyfert 1 galaxy. NGC 4051 has been extensively studied for its variable X-ray emission and the presence of WAs. Krongold (2007) identified two ionization states of WAs in NGC 4051, highlighting the complexity of these outflows. Subsequent studies by Silva et al. (2016) and Ebrero et al. (2016) further analyzed the variability of these absorbers by comparing the fitted strengths of absorption features to solutions to the equations for the time dependence of the dominant ions.

This work attempts to answer the following questions: How does the ionization state of the warm absorber in NGC 4051 vary with changes in the ionizing flux? Is there a correlation between the ionizing flux and the warm absorber properties? If so, is there a detectable lag between the ionizing flux variations and the ionization state response? and what does the lag, if any, tell us about the intrinsic properties of the NGC4051 WA, such as the density? A result of this work, even if the search for correlated and lagged ionization is negative, is that we can define the characteristics of data that are needed in order to perform such searches. Even if such data is not currently available, it is likely that future observatories will be capable of providing it.

The structure of the paper is organized around the questions above. The paper is organized as follows: In section 2, we discuss the observation, data reduction, and analysis, including modeling of the warm absorber using the analytical model, WARMABS (Kallman & Bautista 2001). We present the results of spectral fitting and correlation analysis in section 3, followed by the discussion, conclusion, and future prospect in sections 4, 5, and 6, respectively.

2. OBSERVATION, DATA REDUCTION, AND ANALYSIS

2.1. Observation

Our procedure for using time dependent photoionization modeling to study warm absorbers separates into steps: (i) Dividing the time series of spectra into intervals such that each interval contains sufficient counts to detect a warm absorber, while at the same time maxi-

mizing the number of usable intervals in order to search for variability on the shortest possible timescales; (ii) Fitting each of the intervals to a warm absorber model using a uniform fitting procedure; (iii) Performing simulations in order to characterize the sensitivity of the spectral fits to changing conditions in the warm absorber, i.e. determining how large a change in ionization parameter or column density can be detected; (iv) Performing a cross-correlation analysis to search for correlated variability between the warm absorber parameters and the continuum flux, and for lags between the two time series; and (v) performing the same analysis using a simulation of the entire time series and comparison of this with the analysis from step (iv).

Nicer observations of AGNs such as NGC 4051 typically consist of many individual pointings, with approximately contiguous exposure times ~ 1000 s within each. An observation consists of many pointings, each separated by longer intervals (~ 4500 s) due to earth occultation or the SAA. For the purpose of this paper we selected one NICER observation, from OBSID 1112010115, observed on 2018-01-15, for NGC 4051. The details of this observation is given in the table 1 and visualized in figure 2. The second and third columns represent the starting and stopping times for a particular pointing, the fourth column gives the exposure for this pointing, and the last column represents the gap between two consecutive pointings greater than 700 s. These gaps are ~ 4500 s. The pointings and the gaps are shown in figure 2. The telescope was pointed to the source 28 times during the whole observation. The exposure time ranged from a few seconds to a thousand seconds. For our work, we chose only those pointings with exposure greater than 700 s and discarded all other pointings. This filtering criterion gives us 15 different spectra, from 15 pointings, each with exposure of ~ 1000 s or greater.

The data was reduced using the standard NICER pipelines, `nicerl2`, and the cleaned event files were obtained. Then, we used `maketime` the `heasoft` command to make a good time interval (`gti`) file for each observed segment greater than 700 s exposure and ran `nicerl3-spect` for each one of them, which generated the final spectral products ready for scientific analysis. The latest calibration file (20240206) has been used to reduce the data. The spectra in the case of NICER are binned automatically using the default method of optimal binning (Kaastra & Bleeker 2016) when `nicerl3-spect` is run and used `cstat` while fitting the spectra. Throughout this paper, `cstat` is used for finding the best fits. However, when quoting results, we use χ^2 owing to its simpler interpretation in terms of chance probabilities.

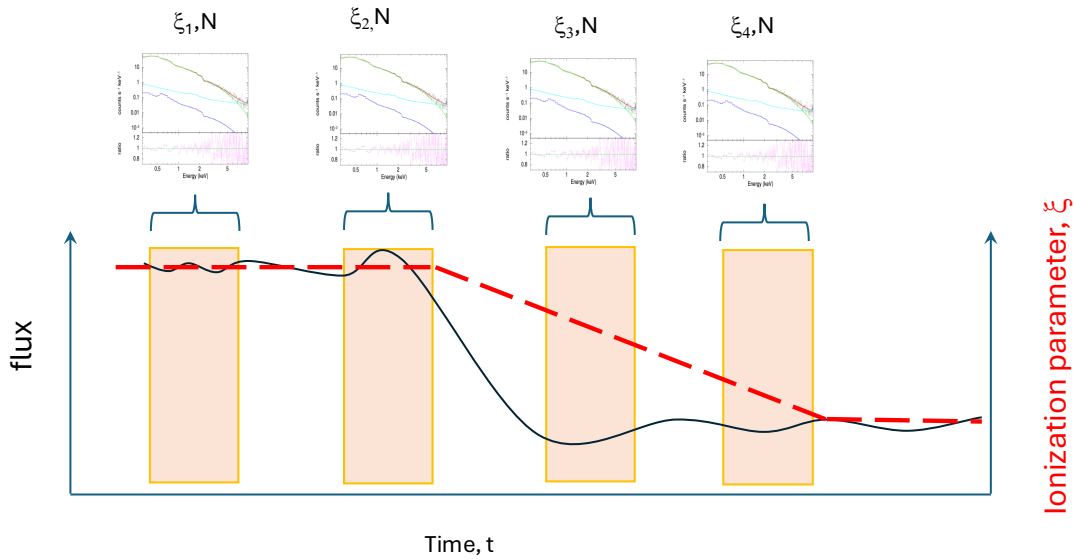


Figure 1. Schematic drawing showing our procedure for studying time-dependent ionization. We divide the observation into intervals and fit for the ionization parameter vs. time (as shown by the red curve) and test for correlation between the change in the ionization parameter and the flux (shown as the black curve). We interpret the lag between the change in the continuum vs. the ionization parameter as the ionization or recombination time. The hatched regions denote the time intervals needed in order to accumulate spectra capable of measuring the ionization parameter.

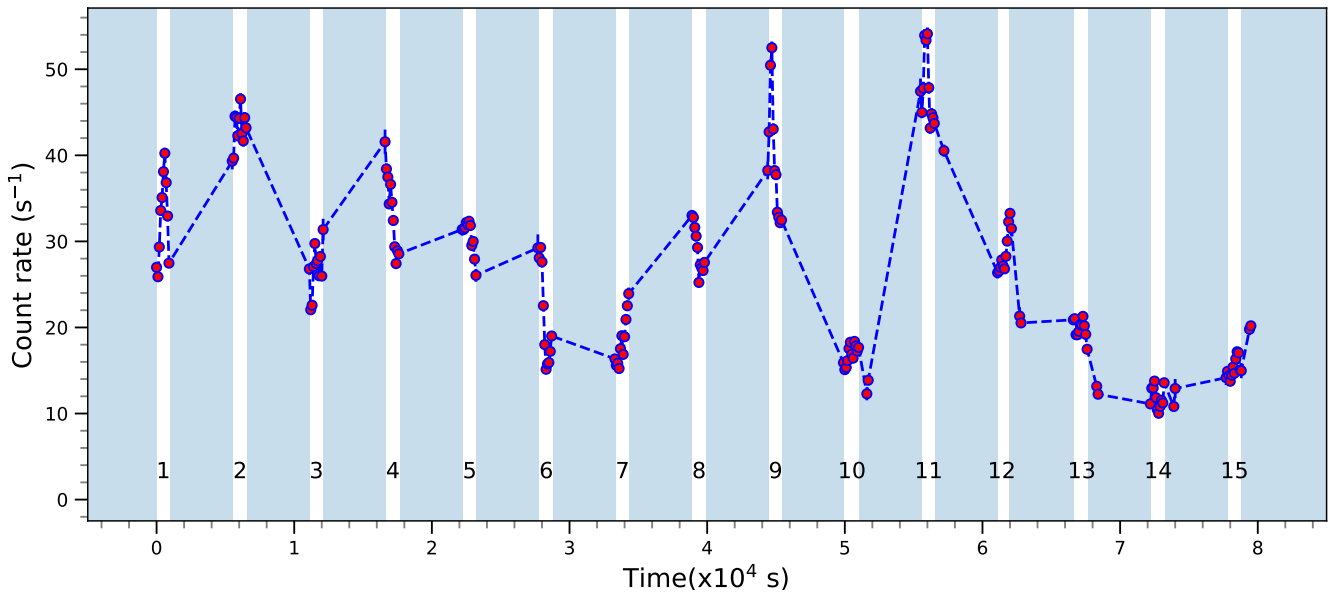


Figure 2. The light curve corresponding to observation ID 1112010115 for NGC 4051. The data gaps are shown in blue bands; each data group is given a number from 1 to 15. The light curve is binned with 100 s. Only those time points that fall in the white region are considered. A few points that fall in the blue region are excluded from our analysis.

The goal of this work is to detect time variability in a warm absorber and then look for correlations between the time series of the warm absorber properties (ionization parameter and column density) and the continuum flux. In order to do so, we strive to maximize the total time duration of the time series of spectra that we analyze, and we also seek typical variability in the ionizing flux of a factor of ~ 3 or more between pointings. This

particular observation exhibits such behavior. This is important because we want to see the response of the gas to the extreme variability of the source luminosity.

The light curve for this observation is shown in the first panel of figure 5. The count rates range from a minimum of ~ 15 counts s^{-1} at a time 5.5×10^4 s to a maximum of ~ 50 counts s^{-1} at a time 6.0×10^4 s. This fulfills the criterion of significant variation in a short

index	start time (s)	stop time (s)	exp. (s)	gap (s)
1	127443371	127444364	993	4562
2	127448926	127449941	1015	4545
3	127454486	127455485	999	4563
4	127460048	127461042	994	4565
5	127465607	127466621	1014	4536
6	127471157	127472181	1024	4528
7	127476709	127477721	1012	4548
8	127482269	127483281	1012	4552
9	127487833	127488841	1008	4481
10	127493322	127494384	1062	4563
11	127498947	127499961	1014	4549
12	127504510	127505269	759	4711
13	127509980	127511081	1101	4546
14	127515627	127516641	1014	4527
15	127521168	127522182	1014	—

Table 1. The start time, stop time, exposure, and the gap between consecutive pointings that are greater than 700 s. For example, for the first pointing, the telescope starts to observe at 127443371 s and ends at 127444364 s with a total exposure of $t = 993$ s, and then there is a break in the observation for gap= 4562 s. The gaps are the times when the telescope does not observe the source.

timescale. The time separation between the points corresponds to the time between pointings, $\simeq 4500$ s. At the time of the minimum flux, the change of luminosity forms a pattern similar to a flare but in the opposite direction, which we call dimming.

2.2. NICER Data Analysis and Warm Absorber Modeling

Spectra were fitted in the (0.3 - 10) keV range. Since NICER does not have an imaging detector, the backgrounds were estimated using the Scorpean model. We fitted all the fifteen time-resolved spectra using XSPEC (Arnaud 1996) using a single component warm absorber outflow model, `tbabs×warmabs×(bbody+powerlaw)`. Where the `tbabs` is the extinction by the neutral gas in our own galaxy, `warmabs` is for the absorption from the ionized gas, `bbody` is continuum emission that comes presumably from the accretion disk close to the black hole and `powerlaw` is the continuum emission from the corona of the source. The galactic absorption is taken to be $1.20 \times 10^{20} \text{ cm}^{-2}$ (HI4PI Collaboration et al. 2016). We include data in the 0.30 to 10 keV energy range due to significant noise outside this range.

The warm ionized gas absorption in the observed spectra is modeled using the analytic model WARMABS (Kall-

man 2024)¹ This model allows XSPEC to simulate warm absorbers without requiring users to construct their own XSTAR input or output tables. This approach relies on precalculated "population files," which are standard XSTAR (Kallman & Bautista 2001) output files. Using these files, the `warmabs` model can directly produce the absorption in synthetic spectra, skipping the complex steps involved in solving rate equations, which is the main time-consuming component in XSTAR. For this project, we have used the population file generated with the spectral energy density (SED) generated by a simple power law with a power law index (Γ) of 2 and included 1000 strongest absorption lines and absorption edges for fitting the spectrum. The (Γ) is similar to what we obtained from the continuum fitting for this source, NGC 4051.

The best fit parameter values are presented in the results section below, and plots for those parameters are given in Figure 5. Using these fitted parameters, we then calculate the cross-correlation and possible lag between the variability of the ionizing source flux and the ionization state of the outflow.

We note that this time lag has a different physical interpretation from the lag that is frequently used to describe the light travel time between spectral components in AGN, such as in reverberation mapping (Blandford & McKee 1982; Kaspi et al. 2000; Peterson et al. 2004).

The cross-correlation is obtained using the following equation:

$$C(\tau) = \sum_t \left[\frac{X(t) - \langle X \rangle}{\sigma_X} \right] \left[\frac{Y(t + \tau) - \langle Y \rangle}{\sigma_Y} \right] \quad (1)$$

Where $C(\tau)$ is the cross-correlation function at time lag τ . $X(t)$ and $Y(t)$ are the two signals being compared, normalized by subtracting their means and dividing by their standard deviations. $\langle X \rangle$ and $\langle Y \rangle$ are the mean values of $X(t)$ and $Y(t)$, respectively. σ_X and σ_Y are the standard deviations of $X(t)$ and $Y(t)$, respectively. τ is the time lag (time shift between the two signals).

2.3. Detection of warm absorbers with NICER

In this section, we explore the strength of the absorption that the NICER instrument can detect and what level of significance can be attained. The key parameters describing the warm absorber are the ionization parameter and the column density. We synthesized two fake spectra using the model, `tbabs×warmabs×(bbody+powerlaw)` using the `fakeit none` command in Xspec. We chose the power law index to be

¹ available from the webpage

<https://heasarc.gsfc.nasa.gov/docs/software/xstar/xstar.html>

$\Gamma = 2$, and a blackbody temperature of 0.10 keV was chosen for the model. The flux from the source was chosen to be $\sim 4.45 \times 10^{-11}$ erg cm $^{-2}$ s $^{-1}$, which is comparable to what we observe from NGC 4051 (Krongold 2007).

We create fake data assuming an exposure time of 1000 s, keeping the WA column constant at 2.6×10^{21} cm $^{-2}$. Two spectra were generated for $\log(\xi) = 0.8$ and 2.0. The obtained spectra were then fitted with and without warm absorbers. Comparing fits with and without warm absorbers, we found $\Delta\chi^2 \simeq 42$ for gas with $\log(\xi) = 0.8$ and $\Delta\chi^2 \simeq 13$ for gas with $\log(\xi) = 2.0$. This value can be compared with $\Delta\chi^2 = 10$ which is the conventional 99% confidence value (Avni 1976) This shows that detecting a warm absorber is more robust for a relatively lower ionized outflow, given the column density remains the same. This experiment resembles what we find in NGC 4051, in which the column density remains more or less constant but changes in the ionization states to respond to the continuum variation. This simulation was for a relatively low column density; for a larger column, comparable or greater sensitivity to the presence of a warm absorber is obtained.

In addition to the above simulation, we have added a contour plot of the ionization parameter and column density of the warm absorber for the simulated spectra with the same continuum taken above and with a smaller column density, 2.0×10^{21} cm $^{-2}$ and $\log(\xi) = 2.0$, as shown in figure 3. This demonstrates NICER can detect and constrain the warm absorber with column density, 2×10^{21} cm $^{-2}$ and $\log(\xi) \sim 2$ for the exposure of 1000 s with 99 percent confidence. And any non-detection of warm absorbers is not the result of limitations of the instrument sensitivity for the parameter space shown in Figure 3.

2.4. Spectral Fitting

The sensitivity of NICER spectra to warm absorbers is displayed in figure 4. This shows the difference between the spectrum fitted with and without the ionized absorber. The figure on the left is fitted with a model `tbabs(bbody+powerlaw)` while on the right it is fitted with `tbabs×WARMABS(bbody+powerlaw)`. The fit is improved with a warm absorber, which is seen visually in the ratio panels below one keV. For this particular spectrum, the addition of the warm absorber produced $\Delta\chi^2 \sim 42$. The best-fit parameters are presented in Table 2 for all spectra. The inclusion of a warm absorber improves the fit in most of the time-resolved spectra. The $\Delta\chi^2$ were greater than 10 in 9 of the spectra and less than 10 for the rest, as shown in the last column of Table 2.

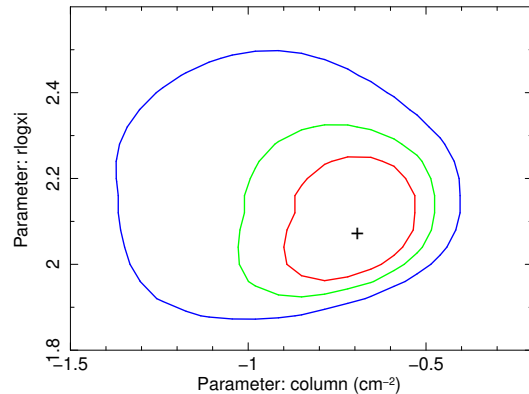


Figure 3. Contour plots of warm absorbers parameters $\log(\xi)$ and column density obtained by fitting the simulated spectra with column density, 2.0×10^{21} cm $^{-2}$ and $\log(\xi) = 2.0$. Red, green, and blue correspond to the 68%, 90%, 99% confidence regions. X axes are converted to a column density as 10^{22-a} , where a is the number in the x-axis. The '+' sign corresponds to $10^{22-0.7}$. This is equivalent to 2×10^{21} cm $^{-2}$.

3. RESULTS

This section presents the results obtained from fitting all 15 time-resolved spectra, including their fit parameters, cross-correlation between flux variation and the ionization structure, time lag, and density and location calculation.

3.1. Fit Parameters

Table 2 summarizes the fit results and is visualized in Figure 5. The spectra all have exposure times $\simeq 1000$ s except the 12th spectrum, which has an exposure of 758 s. The time column in this table is scaled so that the zero corresponds to the start of the first pointing for this obsid.

The fit statistics, which are given in the χ^2/dof column of table 2, show that most of the spectral fits have reduced $\chi^2 \simeq 1$. The continuum fit parameters, such as blackbody temperature kT (keV) and power law index Γ and its error bars, are shown in Table 2. The blackbody temperature ranges from 0.10 to 0.13 keV, and Γ ranges from 1.77 to 2.42, including errors. The `warmabs` model has two free parameters that are most important: column density (N_H) and ionization parameter (ξ). These fit parameters are tabulated in Table 2. The $\Delta\chi^2$ is the difference in the χ^2 when spectra are fitted with and without the warm absorber. This shows the statistical threshold for detecting warm absorbers in the time-resolved spectra. The confidence interval (error bars) of each fitted parameter shown here is 90%.

Figure 5 displays the fitted parameters for all 15 spectra, including the light curves. We have numbered the

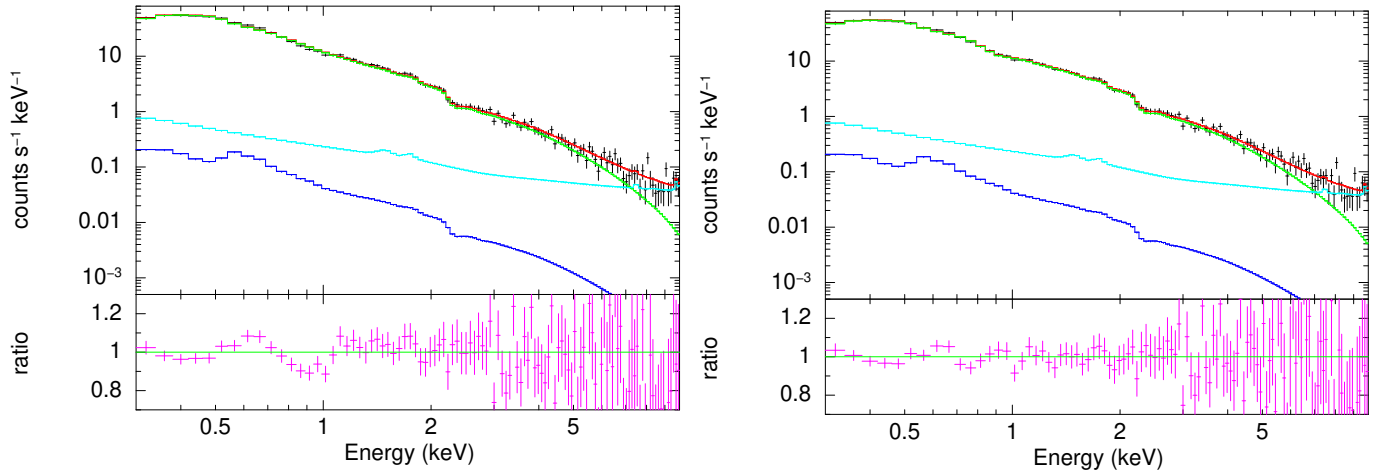


Figure 4. Xspec fit of a spectrum labeled as 1 in our index, which has an exposure of 993 s. Left panel: fitted with model `tbabs(bbody+powerlaw)`. Right panel: fitted with a model `tbabs×WARMABS(bbody+powerlaw)`. Color code: black points are data, the red curve is the model including background and source model, the green curve is the source model, the cyan color curve is non-sky background, the blue color is sky background, and pink points are the ratio plot. The fit was improved significantly with the addition of the warm absorber. The $\Delta\chi^2 \sim 42$ for this particular fit.

pointings 1 to 15. The first two panels represent the count rate in units of s^{-1} and the log of ionizing flux from 0.3 - 10 keV ($\text{ergs s}^{-1} \text{cm}^{-2}$), respectively. The light curve shows a substantial flux variation in a short period. The flux values are 2.5×10^{-11} and 8.0×10^{-11} at points 10 and 11, respectively, a factor of ~ 3 change in the period of ~ 4500 s.

The light curve is highly variable from $\sim 4.5 \times 10^4$ s to $\sim 6.0 \times 10^4$ s as seen in the first and second panels of figure 5. The counts are at a high state at the 9th point and reach a minimum in $\sim 5.0 \times 10^4$ s. It stays there for approximately 1000 s and returns to a high state at 5.5×10^4 s. It stays at a high level for 1000 s and gradually goes towards the low flux states.

The third and fourth panels show the warm absorber parameters, the log of the ionization parameter $\log(\xi)$ in the unit of erg cm s^{-1} and the column density (N_{H}) in the unit of 10^{22}cm^{-2} respectively. The warm absorbers were detected with the column density (N_{H}) ranging from $2 \times 10^{21} \text{cm}^{-2}$ to $4 \times 10^{21} \text{cm}^{-2}$ and the ionization parameter $\log(\xi)$ was found to be 1.89 to 2.85 erg cm s^{-1} with corresponding error bars. We note that column density was not constrained for spectrum number 10 and the ionization parameter for spectrum number 14 with a 90% confidence interval, as seen in figure 5. The contours in figure 8 show the parameters could be constrained with only 68% confidence. Possible explanations for this will be discussed in the following subsections. The bottom two panels are for continuum fit parameters: blackbody kT (keV) and power law index (Γ).

3.2. Correlation Between Flux and Ionization Parameter

Figure 6 shows the correlation between the change in the ionizing flux, i.e. the continuum flux, and the fitted ionization parameter. The solid green line is the best fit regression line for this data set. All the data points lie approximately on this line, accounting for error bars, with the exception of pointing number 10. This shows the ionization structure of the ionized gas approximately follows the change in the flux. This means the lower the ionization, the lower the source flux, and vice versa. Pointing 10 is significantly away from the best-fit line. It is worth noting that the best fit ionization parameter for this pointing is greater than the ionization parameter values for the other pointings, while at the same time the total flux in this pointing is among the lowest. This suggests that the number of counts in this pointing is too low to allow accurate measurement of the warm absorber parameters. Nonetheless, we incorporate the results of fitting to this pointing into our subsequent analysis.

3.3. Cross-Correlation, Time Lag

To investigate the possible time-dependent photoionization signature in more detail, we perform cross-correlations between flux and the ionization parameters at different lags using equation 1.

Figure 7 displays the cross-correlation coefficient vs. lag. The top panel shows the flux variation, the middle panel shows the time evolution of the ionization parameter, and the bottom panel shows the cross-correlation between these two quantities vs. lag. Based on the data and the fit parameters we obtained, there is a maximum positive correlation at -5500 s. This is marked by a pink vertical line A in the last panel of figure 7. This means the ionization is lagging behind the flux variation

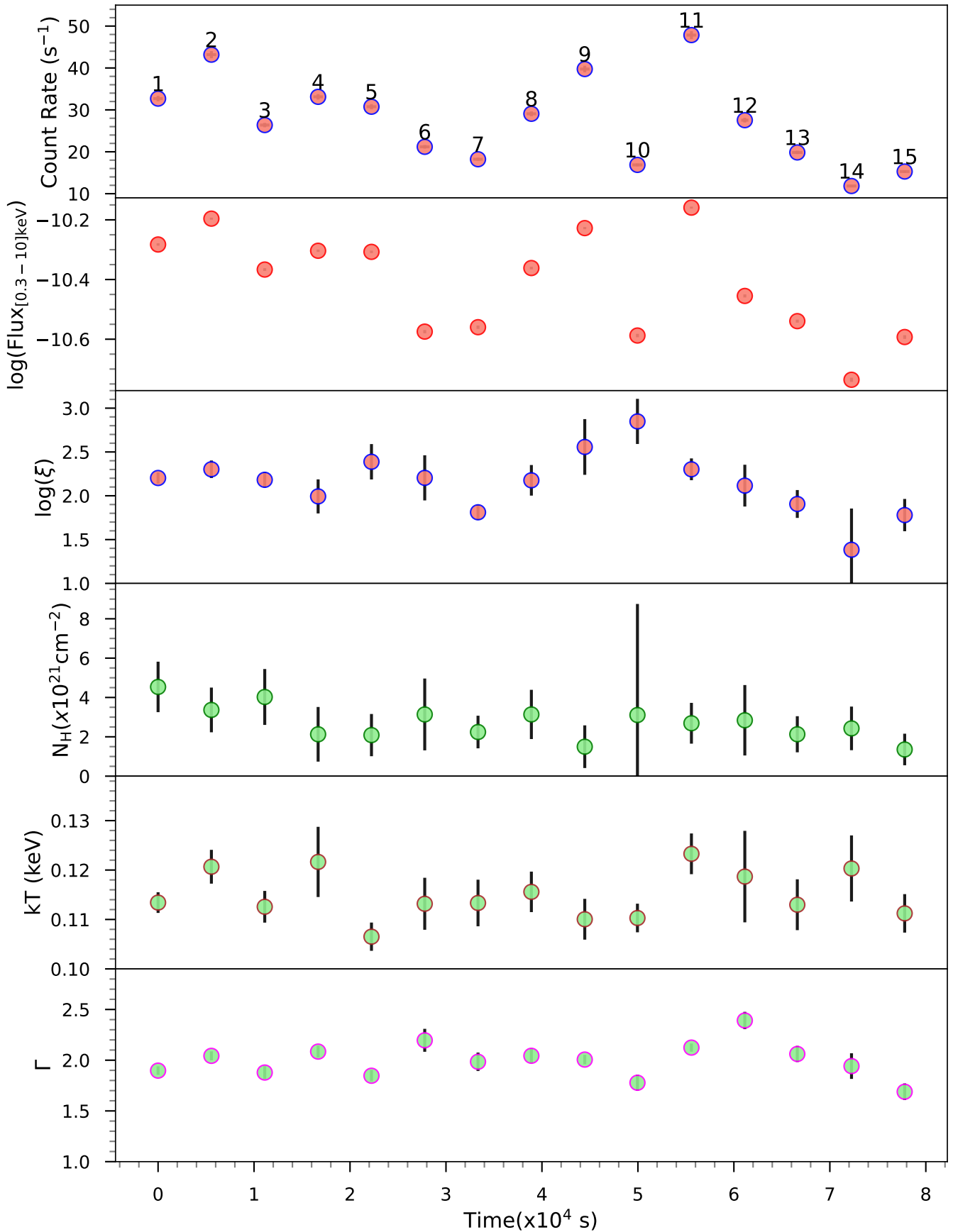


Figure 5. The figure shows the different fitted parameters with their corresponding error bars on the y-axis and time on the x-axis. The exposure time for each spectrum is ~ 1000 s. Each data point in the first panel is labeled with numbers 1 to 15 shown in the first panel.

sn	time (s)	exposure (s)	count rate (s^{-1})	N_{H} ($\times 10^{21} \text{cm}^{-2}$)	$\log(\xi)$	kT (keV)	Γ	χ^2/dof	$\Delta\chi^2$
1	0	992	32.69 ± 0.65	4.54 ± 1.28	2.20 ± 0.06	0.11 ± 0.00	1.90 ± 0.04	116/104	42.43
2	5555	1014	43.18 ± 0.86	3.37 ± 1.14	2.30 ± 0.10	0.12 ± 0.00	2.04 ± 0.04	150/105	27.22
3	11115	998	26.38 ± 0.53	4.02 ± 1.42	2.18 ± 0.09	0.11 ± 0.00	1.88 ± 0.06	117/103	24.72
4	16677	993	33.12 ± 0.66	2.13 ± 1.39	1.99 ± 0.19	0.12 ± 0.01	2.08 ± 0.06	111/105	12.59
5	22235	1013	30.76 ± 0.62	2.09 ± 1.07	2.39 ± 0.20	0.11 ± 0.00	1.85 ± 0.06	111/107	7.93
6	27786	1023	21.19 ± 0.42	3.14 ± 1.83	2.20 ± 0.26	0.11 ± 0.01	2.20 ± 0.11	128/105	6.11
7	33338	1011	18.22 ± 0.36	2.24 ± 0.83	1.81 ± 0.09	0.11 ± 0.00	1.98 ± 0.09	123/102	10.08
8	38898	1011	29.07 ± 0.58	3.14 ± 1.25	2.18 ± 0.17	0.12 ± 0.00	2.04 ± 0.07	120/104	15.05
9	44462	1007	39.74 ± 0.79	1.50 ± 1.08	2.56 ± 0.32	0.11 ± 0.00	2.01 ± 0.05	144/105	5.83
10	49951	1061	16.87 ± 0.34	3.11 ± 5.65	2.85 ± 0.26	0.11 ± 0.00	1.78 ± 0.08	120/100	2.89
11	55576	1013	47.85 ± 0.96	2.69 ± 1.04	2.30 ± 0.12	0.12 ± 0.00	2.12 ± 0.04	126/105	22.29
12	61139	758	27.54 ± 0.55	2.84 ± 1.79	2.12 ± 0.24	0.12 ± 0.01	2.39 ± 0.09	150/98	2.07
13	66609	1100	19.84 ± 0.40	2.13 ± 0.92	1.91 ± 0.16	0.11 ± 0.01	2.06 ± 0.08	124/101	13.50
14	72256	1013	11.83 ± 0.24	2.43 ± 1.11	1.38 ± 0.47	0.12 ± 0.01	1.94 ± 0.13	89/97	10.54
15	77797	1013	15.29 ± 0.31	1.36 ± 0.80	1.78 ± 0.18	0.11 ± 0.00	1.69 ± 0.08	88/99	3.87

Table 2. details about the individual spectrum, including the fit parameters. Each spectrum was fitted using model `tbabs×WARMABS(bbody+powerlaw)`.

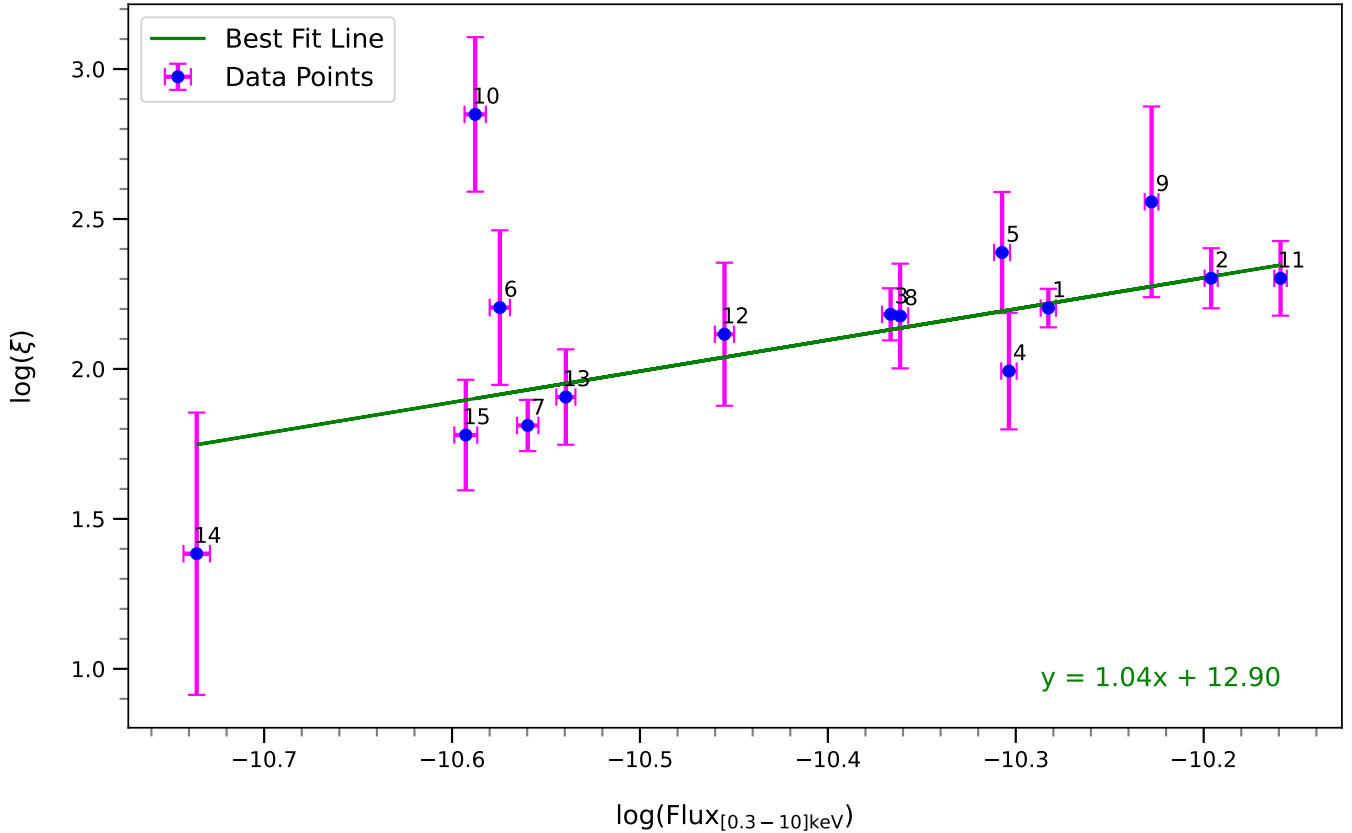


Figure 6. Figure showing how the ionization parameter correlates with $\log(\text{flux})$. The unit of flux is $\text{erg cm}^{-2} \text{s}^{-1}$. The green line represents the best-fit model. This means that if the gas were in an equilibrium state, the data point should touch this line within the margin of error. The data pointing 10 is away from this line, possibly due to insufficient warm absorber signal to allow sensitive fitting.

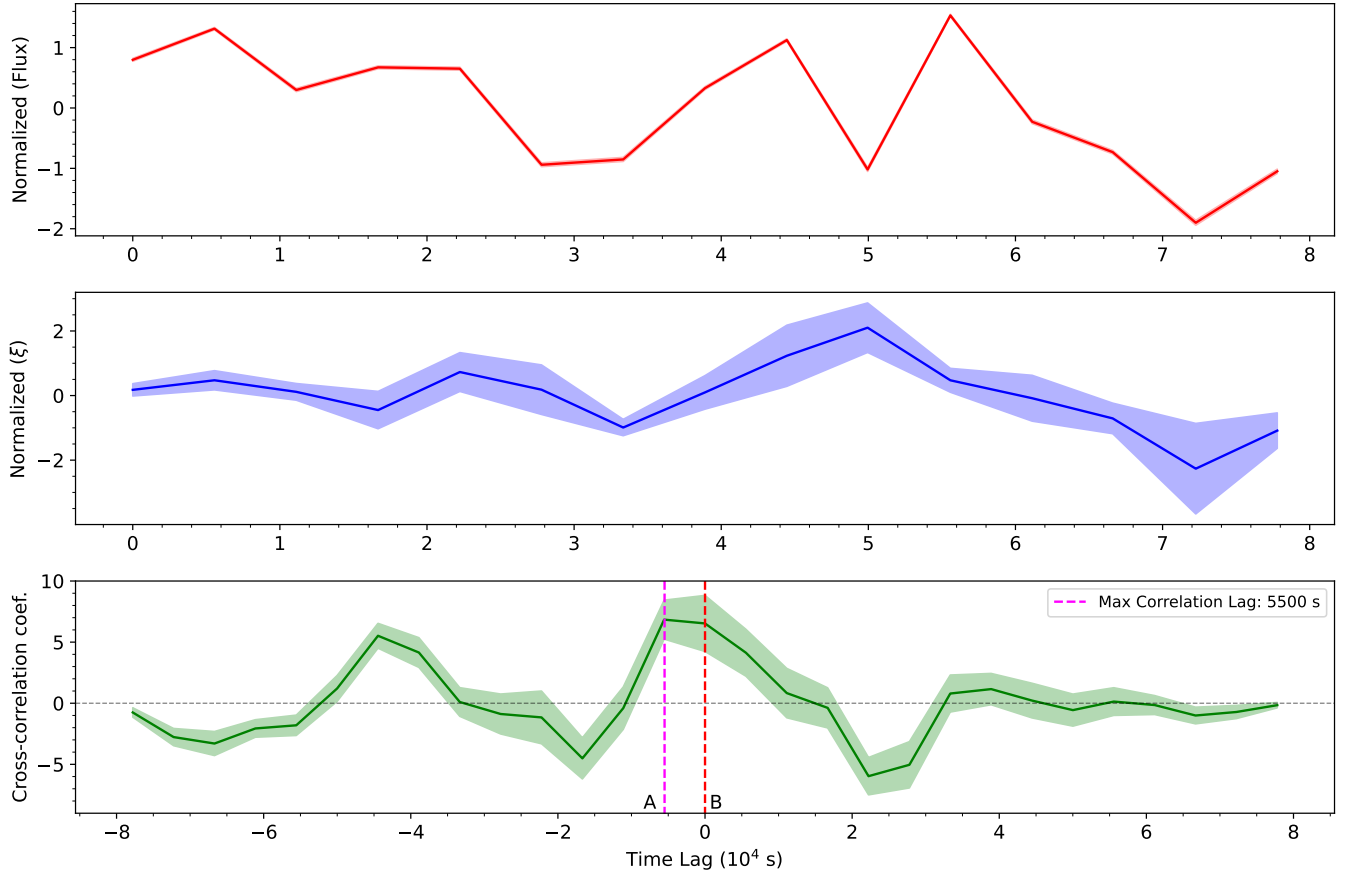


Figure 7. First panel: The normalized light curve and its associated error bars. Second panel: The normalized ionization parameters and associated errors. Third panel: Cross-correlation at different lags between flux and ionization parameters. The curves are not smooth because of the smaller number of sampling points. We have here only 15 points. The time resolution is ~ 5500 s, and the accuracy is limited by the NICER instrument. We calculated the error bar on the cross-correlation coefficient using the Monte Carlo simulation. The maximum correlation coefficient is ~ 7.5 at ~ 5500 s, point A in the figure. However, if you consider the error bars, the zero time lag cannot be ruled out, which is point B in the figure and represented by a red dashed vertical line. So, the time lag can be anything in between magenta and red vertical lines.

by ~ 5500 s and suggests a time delay in the response. We infer that the gas may be out of photoionization equilibrium during this period. Even though the cross-correlation shows a maximum at the time lag ~ 5500 s, we cannot rule out the time lag of zero if we consider the error in these values, which is marked by a red vertical line B in the last panel of figure 7. That is, the region allowed by the 90% error bars includes zero lag with the same level of correlation as for the 5500 s lag. This prevents us from setting a firm upper limit on the density based on the cross-correlation coefficient; we can only calculate a lower limit on the density corresponding to the time lag ~ 5500 s. If the value of the time lag is small, near zero, the gas is effectively in equilibrium for all of our pointings, given the time resolution we have.

3.4. Error Estimation in Cross-correlation

The dark lines in Figure 7 represent the measured values, while the shaded regions indicate the associated errors on the cross-correlation function. The data between the points were interpolated to provide a continuous representation. While the error bars for the flux and ionization parameters were directly derived from the spectral fitting, uncertainties in the cross-correlation function were derived from simulations.

The error bars in the cross-correlation, shown as the green shaded region in the bottom panel of Figure 7, were calculated using Monte Carlo simulations. The cross-correlation itself is determined from the two sets of best-fit values of the quantities being correlated and does not inherently account for the uncertainties in the fitted parameters. To address this, we generated 10,000 simulated light curves and ionization curves by randomly sampling values within the error bars of the fitting parameter, i.e., the ionization parameter. For each pair

of simulated light and ionization curves, we computed a cross-correlation, resulting in 10,000 correlation curves. The green-shaded region represents the envelope of these 10,000 correlation curves, effectively capturing the uncertainties in the cross-correlation.

3.5. Time-Evolving Photoionization

Results shown in figure 7 constrain the range of time during which the ionization balance in the gas may be out of equilibrium. Equation 2 shows how these results are connected to the interesting quantities affecting the gas, i.e., the density and ionizing flux. This equation defines the equilibrium timescale $t_{\text{eq}}^{X_i, X_{i+1}}$, which measures the time required for an ion to reach ionization equilibrium with the ionizing continuum. This equilibrium timescale is crucial in understanding the response of ionized gas to changes in the ionizing flux, particularly in gas near accreting compact objects, such as in active galactic nuclei (AGN).

$$t_{\text{eq}}^{X_i, X_{i+1}} = \frac{1}{n_e \alpha_{\text{rec}}(T_e) + \gamma_{\text{PI}}} \quad (2)$$

In this equation, $t_{\text{eq}}^{X_i, X_{i+1}}$ represents the time needed for the ionization state of a specific ion X_i to adjust to the ionizing conditions at a given moment. This timescale depends on the following variables:

- $\alpha_{\text{rec}}(X_i, T_e)$: The radiative recombination coefficient for the ion X_i at the electron temperature T_e . This coefficient measures the rate at which the ion X_i recombines with free electrons to form the ion X_{i-1} .
- n_e : The electron density in the gas. Higher electron densities lead to shorter recombination times, thereby reducing the equilibrium timescale.
- γ_{PI} : The photoionization rate of the ion X_i in the gas.

The terms on the right-hand side correspond to the inverse of the recombination timescale if the photoionization rate is small, or the inverse of the photoionization timescale if the recombination rate is small. These determine how quickly the gas can return to equilibrium after a sudden change in the ionization rate.

This timescale t_{eq} is fundamental in the study of AGN outflows and warm absorbers, where the gas is often subject to rapid changes in ionizing flux. In low-density environments, the recombination timescale can be much longer than the timescale of changes in the ionizing continuum, leading to a situation where the ionization state

of the gas is continuously out of equilibrium. This non-equilibrium state can result in observable effects, such as delayed responses in the ionization state relative to changes in the ionizing source, as well as the overionization of the gas compared to the predictions of simple equilibrium models.

3.6. Density Calculation

The gas response to the change in the ionizing flux changes its ionization state. Adjusting the gas ionization structure depends on a few fundamental quantities. They are: how fast the ionizing flux changes, how significant those changes are, and the photoionization and recombination time scale. The ionization and recombination timescales play a crucial role in this entire process, which depends on the density and temperature of the gas.

No.	Ion	Abund	Rec. Rate Coef. ($\text{cm}^3 \text{s}^{-1}$)	Ion. Rate (s^{-1})
1	O VI	1.99E-03	6.69E-12	1.02E-02
2	O VII	2.98E-01	1.67E-11	1.91E-04
3	O VIII	5.16E-01	1.46E-11	5.19E-05

Table 3. Abundance here is ionic abundance (Abund) relative to the elemental abundance. The recombination rate coefficient (Rec. Rate Coef.) refers to radiative recombination, and the ionization rate (Ion. Rate) refers to the photoionization rates for various ions. These values are obtained by running equilibrium XSTAR for the input parameters similar to this source, which are $\Gamma = 2$, $\log(\xi) = 2.56$ and luminosity of $4.38 \times 10^{42} \text{ erg s}^{-1}$.

The time lag in the correlation curve gives the minimum time required for the cloud to come to equilibrium. This equilibrium time is used to approximate the gas density that is out of equilibrium using equation 2. So, using equation 2, we can find the electron density of an outflow considering the fact that most of the absorption comes from oxygen ions since most of the absorption in the warm absorber comes from oxygen (Sadaula & Kallman 2024). We consider O VIII ion for our calculation because more than 50% of the ions are in this ion stage under the conditions of the warm absorbers in NGC 4051. The equilibrium recombination rate coefficient and photoionization timescales are listed in Table 3. Using these values and the time lag mentioned previously, we found that the lower limit of electron density is $\simeq 8.91 \times 10^6 \text{ cm}^{-3}$ corresponding to the time lag of $\simeq 5500 \text{ s}$.

We calculate the photoionization rate and recombination rate coefficients using equilibrium XSTAR, considering input parameters similar to this source. We considered the ninth point as a reference because the

gas did not follow the flux variation at point 10, likely departing from equilibrium. The source at point nine is characterized as, $\sim \Gamma = 2.0$, $\log(\xi) \sim 2.5$ and measured unabsorbed flux in (0.3 - 10) keV 6.31×10^{-11} erg $\text{cm}^{-2} \text{s}^{-1}$. The corresponding luminosity in the range 1-1000 Ryd of the source after the bolometric correction based on the AGN spectral energy density (SED), which is taken to be 2, is 4.38×10^{42} erg s^{-1} . We calculated 1-1000 Ryd luminosity because XSTAR requires the input luminosity in the energy range of 1-1000 Ryd. We get the temperature of $\simeq 7 \times 10^4$ K and the recombination rate coefficient (α) and photoionization rate γ for oxygen as given in Table 3 from XSTAR for the above input parameters.

Using the gas density estimates we have calculated, we can approximate the location of the warm absorbers using the equation $\xi = L_X/(n_e r^2)$ where ξ is the ionization parameter, L_X is the ionizing luminosity, n_e is the electron density, and r is the distance of the absorber from the ionizing source (Tarter et al. 1969). Using the parameter values above, we find that the maximum possible distance of the warm absorber from the black hole corresponding to the density $8.91 \times 10^6 \text{ cm}^{-3}$ is $\simeq 7.02 \times 10^{16} \text{ cm}$ or 0.023 pc.

4. DISCUSSION

In this work, we have studied the response of the ionized outflow to the change in the ionizing continuum of the central region in AGN. For this, we have chosen NGC 4051, which is a nearby Syfert 1 galaxy. Many studies have found the existence of the warm absorber in this source (Krongold 2007; Laha et al. 2014). Since NICER has a high effective area at the soft x-ray band ~ 1 keV, and the absorption feature of the warm absorber is also found in a similar energy range, we have used NICER data despite its limited energy resolution.

We chose a NICER observation of ~ 16000 s net exposure time for this source. We chopped the data into 15 segments, each with an exposure of ~ 1000 s with a ~ 4500 s gap between consecutive pointings. Each pointing is given a number from 1 to 15, as shown in Figure 2 (the white space between the blue regions), and fitted to the model `tbabs×WARMABS(bbody+powerlaw)`. The fitted parameters are all given in Table 2 and visualized in Figure 5. We have detected and are able to constrain the warm absorber in most of the spectra, except for spectra 10 and 14. We have found the upper limits of ionization parameters and column density for these two spectra with relatively large error bars. The warm absorber ionization structure follows the pattern in the ionizing flux, except pointing 10 (see fig. 6.)

The warm absorber gas column density is found to be in the range of $1.5 \times 10^{21} \text{ cm}^{-2}$ to $4.5 \times 10^{21} \text{ cm}^{-2}$ indicating it remained more or less constant throughout the observation if we consider the error bars. However, the ionization parameter clearly changed when the flux varied. This is expected and meaningful in the physical sense. The cloud persistently changes its ionization structure depending upon the change in the central ionizing source flux. This idea is also corroborated by Krongold et al. (Krongold 2007) using data from the *XMM-Newton* observatory.

The cross-correlation is calculated at different lags for flux and the ionization parameters as given in Figure 7. The correlation is maximum at ~ 5500 s, indicating the cloud is not perfectly at equilibrium during the response to the continuum flux change. However, if we consider the errors on the correlation curve, we can not rule out the possibility that the correlation has zero time lag, indicating the equilibration time is short compared with the pointing separation, 5500 s. We found the upper limit on the possible time lag from the correlation curve to be ~ 5500 s. Using the equation 2, this time lag is translated to the lower limit of the electron density to be $8.91 \times 10^6 \text{ cm}^{-3}$.

Past work on this source has found warm absorbers (WA) in two ionization states: low and high ionization (Krongold 2007; Laha et al. 2014). We only report the high ionization state outflow here in this work. We have calculated the lower limit on the electron density, which is $8.91 \times 10^6 \text{ cm}^{-3}$. This is consistent with findings of Krongold (2007), who find electron density in the range $(5.8 - 21.0) \times 10^6 \text{ cm}^{-3}$.

This work attempts to use the time lag technique to estimate the density of the outflow. However, there are some caveats, which are listed below.

1. We have assumed the stationary ionized outflow. However, in reality, the WA gas has a speed ranging from a few hundred to a few thousand km s^{-1} .
2. When the spectra are fitted in XSPEC, NICER uses a scorpeon model to estimate the background. Running the WARMABS analytical model is somewhat time-consuming in this case. So, we fitted all the spectra using the scorpeon model but froze all the background parameters during the error estimation. This may slightly underestimate the confidence interval for all the model parameters.
3. This work is limited to the minimum time resolution of ~ 5500 s that NICER data can have due to the earth's occultation. The cross-correlation in Figure 7 was obtained by interpolating between

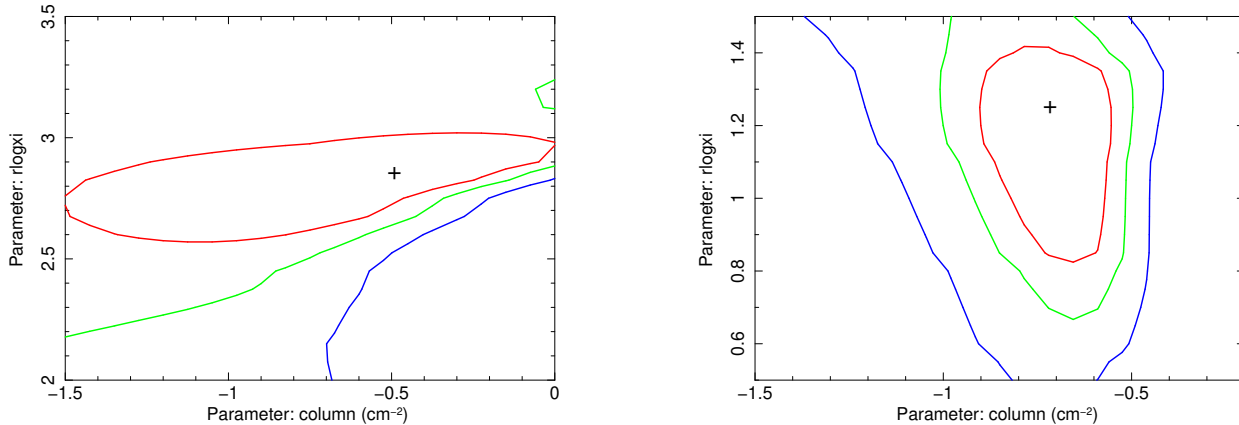


Figure 8. Contour plots of warm absorbers parameters $\log(\xi)$ and column density. Red, green, and blue correspond to the 68%, 90%, 99% confidence regions. X axes are converted to a column density as 10^{22-a} , where a is the number in the x-axis. Left: contour for spectrum number 10. The + sign corresponds to $10^{22-0.5}$. This is equivalent to $\sim 3.1 \times 10^{21} \text{ cm}^{-2}$. Right: contour for spectrum number 14. The + sign corresponds to $10^{22-0.7}$. This is equivalent to $\sim 2.0 \times 10^{21} \text{ cm}^{-2}$. The parameters are well constrained only within the 68 percent of confidence in these two cases.

the data points. This contributes to the error estimation of the time lag and, hence, the density calculation of the gas.

4. We have chosen to use the atomic rates for oxygen ions O VI, O VII, and O VIII for the density calculation, assuming these ions are responsible for most of the absorption. If we consider other ions such as carbon, neon, or iron, the rates will differ. The density limits derived from these rates are likely to be less accurate than what we derive since oxygen is the dominant element responsible for absorption in WAs.
5. The column density and ionization parameter in the pointing number 10 in the figure 5 cannot be constrained to within 68% confidence as shown in the left of the figure 8. We attribute this to the fact that in this pointing the gas was highly ionized, and at the same time the flux went down to the low state. The column cannot be constrained under these conditions, i.e. if there is little absorption and the source is in a low state. On the other hand, the ionization parameter in the pointing number 14 in the figure 5 is constrained with in the 68% confidence as shown in the right of the figure 8. Both these points in the light curve are at low flux state, but they differ in their column density and/or ionization state.
6. The delta chi-square value with and without the warm absorber fit is not highly significant in some of the time-resolved spectra (see the last column of Table 2). This indicates that a warm absorber

is not required to fit some of the spectra. This may be because the absorption is very low due to overionization and/or the source is at a low flux state.

5. CONCLUSION

This study contributes to our understanding of the density and location of warm absorbers in AGN, using a time-lag-based density diagnostic method. It highlights the importance of time-resolved spectroscopy in constraining ionized outflows, which play a role in AGN feedback and galaxy evolution.

The conclusions drawn from the study on the variability of warm absorbers in NGC 4051 using NICER observations are as follows:

1. **Time-Resolved Spectroscopy Capability:** The study demonstrates that NICER can be used to conduct time-resolved spectroscopy of warm absorbers with a time resolution of approximately ~ 5500 seconds, despite its low spectral resolution.
2. **Detection of Warm Absorbers:** The analysis of 15 time-resolved spectra confirms the presence of a warm absorber in most of them, with column densities N_H ranging from $1.5 \times 10^{21} \text{ cm}^{-2}$ to $4.5 \times 10^{21} \text{ cm}^{-2}$ and ionization parameters $\log(\xi)$ varying between 1.89 and 2.85. However, in some spectra, the warm absorber parameters are not well constrained, possibly due to overionization or low flux states.
3. **Correlation Between Ionization and Flux:** The study finds a strong correlation between the ion-

ization state of the warm absorber and the ionizing flux, as expected in photoionization equilibrium. However, spectrum 10 shows a deviation from this correlation, suggesting that the gas was out of equilibrium during that period.

4. **Time Lag and Non-Equilibrium Effects:** A time lag of approximately 5500 seconds is observed between the flux variations and the response of the absorber's ionization state. This indicates that the gas is not in instantaneous photoionization equilibrium and suggests a recombination timescale dependent on gas density.
5. **Lower Limit on Electron Density:** Using the observed time lag, the study estimates the lower limit on the electron density of the warm absorber to be $\sim 8.91 \times 10^6 \text{ cm}^{-3}$. This is consistent with previous studies on this source.
6. **Constraints on the Location of the Warm Absorber:** Given the estimated density, the warm absorber is inferred to be located at a distance $\leq 7.02 \times 10^{16} \text{ cm}$ ($\sim 0.023 \text{ pc}$) from the central black hole.

6. FUTURE PROSPECT

The time evolution of absorption that comes from the coevolution of the supermassive black hole and its host galaxy has been established (Gebhardt et al. 2000; Ferrarese & Merritt 2000) long ago. Understanding the coevolution of the black hole with the host galaxy is important in the context of the evolution of the galaxy and the universe. For this to occur, there should be some way that the SMBH communicates with the host galaxy by giving it back part of the accreting material

in the form of energy and mass. But what the different channels of the feedback are and how it works is still not clearly understood.

The warm ionized absorber is believed to be critical for the AGN in this process. However, the origin and properties of the warm absorber, such as density and location, are still not calculated independently because there is degeneracy in the density and the location. Time-resolved spectroscopy is one of the ways to remove this degeneracy. However, existing technology has still not reached a level where the time-resolved spectroscopy of a few tens to hundreds of seconds is possible. These are the typical times of variation in the AGN continuum, mainly in the X-ray. Spectra obtained with the grating instruments on *XMM-Newton* or *Chandra* do a better job of constraining the WA parameters, but they require much longer exposure to obtain the required level of signal-to-noise. This limits the accessible time resolution. On the other hand, we have demonstrated a novel, indirect way to study warm absorbers and derive densities using the *Nicer* observatory. That is, we look at the time series of model fits to *Nicer* spectra and search for changes in ionization state that are correlated with the continuum, but with a lag. In this way we are able to access variability timescales shorter than those from *XMM-Newton*. However, the timescales accessible to *Nicer* are limited by earth occultations. This provides motivation for future missions that have even greater collecting areas and fewer pointing constraints than *NICER* and so will be capable of searching for time-dependent effects on the truly relevant timescales. This will provide more accurate density limits, along with advancements in warm absorber density constraints.

REFERENCES

- Arnaud, K. A. 1996, in *Astronomical Society of the Pacific Conference Series*, Vol. 101, *Astronomical Data Analysis Software and Systems V*, ed. G. H. Jacoby & J. Barnes, 17
- Avni, Y. 1976, *ApJ*, 210, 642, doi: [10.1086/154870](https://doi.org/10.1086/154870)
- Behar, E., Rasmussen, A. P., Blustin, A. J., et al. 2003, *apj*, 598, 232, doi: [10.1086/378853](https://doi.org/10.1086/378853)
- Blandford, R. D., & McKee, C. F. 1982, *ApJ*, 255, 419, doi: [10.1086/159843](https://doi.org/10.1086/159843)
- Blustin, A. J., Page, M. J., Fuerst, S. V., Branduardi-Raymont, G., & Ashton, C. E. 2005, *A&A*, 431, 111, doi: [10.1051/0004-6361:20041775](https://doi.org/10.1051/0004-6361:20041775)
- Cattaneo, A., Faber, S. M., Binney, J., et al. 2009, *Nat*, 460, 213, doi: [10.1038/nature08135](https://doi.org/10.1038/nature08135)
- Chartas, G., Brandt, W. N., Gallagher, S. C., & Garmire, G. P. 2002, *ApJ*, 579, 169, doi: [10.1086/342744](https://doi.org/10.1086/342744)
- Crenshaw, D. M., Kraemer, S. B., & George, I. M. 2003, *ARAA*, 41, 117, doi: [10.1146/annurev.astro.41.082801.100328](https://doi.org/10.1146/annurev.astro.41.082801.100328)
- Croton, D. J., Springel, V., White, S. D. M., et al. 2006, *MNRAS*, 365, 11, doi: [10.1111/j.1365-2966.2005.09675.x](https://doi.org/10.1111/j.1365-2966.2005.09675.x)
- Di Matteo, T., Springel, V., & Hernquist, L. 2005, *Nat*, 433, 604, doi: [10.1038/nature03335](https://doi.org/10.1038/nature03335)
- Ebrero, J., Kaastra, J. S., Kriss, G. A., et al. 2016, *A&A*, 587, A129, doi: [10.1051/0004-6361/201527808](https://doi.org/10.1051/0004-6361/201527808)

- Elvis, M. 2000, *apj*, 545, 63, doi: [10.1086/317778](https://doi.org/10.1086/317778)
- Fabian, A. C. 2012, *ARAA*, 50, 455, doi: [10.1146/annurev-astro-081811-125521](https://doi.org/10.1146/annurev-astro-081811-125521)
- Ferrarese, L., & Merritt, D. 2000, *ApJ*, 539, L9, doi: [10.1086/312838](https://doi.org/10.1086/312838)
- García, J., Elhoussieny, E. E., Bautista, M. A., & Kallman, T. R. 2013, *The Astrophysical Journal*, 775, 8, doi: [10.1088/0004-637x/775/1/8](https://doi.org/10.1088/0004-637x/775/1/8)
- Gebhardt, K., Bender, R., Bower, G., et al. 2000, *ApJ*, 539, L13, doi: [10.1086/312840](https://doi.org/10.1086/312840)
- Gendreau, K. C., Arzoumanian, Z., Adkins, P. W., et al. 2016, in *Society of Photo-Optical Instrumentation Engineers (SPIE) Conference Series*, Vol. 9905, *Space Telescopes and Instrumentation 2016: Ultraviolet to Gamma Ray*, ed. J.-W. A. den Herder, T. Takahashi, & M. Bautz, 99051H, doi: [10.1117/12.2231304](https://doi.org/10.1117/12.2231304)
- Gu, L., Kaastra, J., Rogantini, D., et al. 2023, *A&A*, 679, A43, doi: [10.1051/0004-6361/202347430](https://doi.org/10.1051/0004-6361/202347430)
- Halpern, J. P. 1984, *ApJ*, 281, 90, doi: [10.1086/162077](https://doi.org/10.1086/162077)
- HI4PI Collaboration, Ben Bekhti, N., Flöer, L., et al. 2016, *A&A*, 594, A116, doi: [10.1051/0004-6361/201629178](https://doi.org/10.1051/0004-6361/201629178)
- Juráňová, A., Costantini, E., & Uttley, P. 2022, *MNRAS*, 510, 4225, doi: [10.1093/mnras/stab3731](https://doi.org/10.1093/mnras/stab3731)
- Kaastra, J. S., & Bleeker, J. A. M. 2016, *A&A*, 587, A151, doi: [10.1051/0004-6361/201527395](https://doi.org/10.1051/0004-6361/201527395)
- Kaastra, J. S., Steenbrugge, K. C., Raassen, A. J. J., et al. 2002, *A&A*, 386, 427, doi: [10.1051/0004-6361:20020235](https://doi.org/10.1051/0004-6361:20020235)
- Kallman, T. 2024, WARMABS. <https://heasarc.gsfc.nasa.gov/docs/software/xstar/docs/sphinx/xstardoc/docs/build/html/warmabs.html>
- Kallman, T., & Bautista, M. 2001, *ApJS*, 133, 221, doi: [10.1086/319184](https://doi.org/10.1086/319184)
- Kaspi, S., Smith, P. S., Netzer, H., et al. 2000, *ApJ*, 533, 631, doi: [10.1086/308704](https://doi.org/10.1086/308704)
- Krolik, J. H., & Kriss, G. A. 1995, *apj*, 447, 512, doi: [10.1086/175896](https://doi.org/10.1086/175896)
- Krongold, Y. 2007, in *The Nuclear Region, Host galaxy and Environment of Active Galaxies*, 21
- Laha, S., Guainazzi, M., Dewangan, G., Chakravorty, S., & Kembhavi, A. 2014, in *The X-ray Universe 2014*, ed. J.-U. Ness, 112
- Li, C., Kaastra, J. S., Gu, L., & Mehdipour, M. 2023a, *A&A*, 680, A44, doi: [10.1051/0004-6361/202346520](https://doi.org/10.1051/0004-6361/202346520)
- . 2023b, *A&A*, 680, A44, doi: [10.1051/0004-6361/202346520](https://doi.org/10.1051/0004-6361/202346520)
- Luminari, A., Nicastro, F., Krongold, Y., Piro, L., & Thakur, A. L. 2023, *A&A*, 679, A141, doi: [10.1051/0004-6361/202245600](https://doi.org/10.1051/0004-6361/202245600)
- Luminari, A., Piconcelli, E., Tombesi, F., Nicastro, F., & Fiore, F. 2024, *arXiv e-prints*, arXiv:2410.13933, doi: [10.48550/arXiv.2410.13933](https://doi.org/10.48550/arXiv.2410.13933)
- Nicastro, F., Fiore, F., Perola, G. C., & Elvis, M. 1999, *ApJ*, 512, 184, doi: [10.1086/306736](https://doi.org/10.1086/306736)
- Peterson, B. M., Ferrarese, L., Gilbert, K. M., et al. 2004, *ApJ*, 613, 682, doi: [10.1086/423269](https://doi.org/10.1086/423269)
- Pounds, K. A., King, A. R., Page, K. L., & O'Brien, P. T. 2003a, *MNRAS*, 346, 1025, doi: [10.1111/j.1365-2966.2003.07164.x](https://doi.org/10.1111/j.1365-2966.2003.07164.x)
- Pounds, K. A., Reeves, J. N., King, A. R., et al. 2003b, *MNRAS*, 345, 705, doi: [10.1046/j.1365-8711.2003.07006.x](https://doi.org/10.1046/j.1365-8711.2003.07006.x)
- Rogantini, D., Mehdipour, M., Kaastra, J., et al. 2022, *ApJ*, 940, 122, doi: [10.3847/1538-4357/ac9c01](https://doi.org/10.3847/1538-4357/ac9c01)
- Rosito, M. S., Pedrosa, S. E., Tissera, P. B., et al. 2021, *A&A*, 652, A44, doi: [10.1051/0004-6361/202039976](https://doi.org/10.1051/0004-6361/202039976)
- Rozanska, A., Goosmann, R., Dumont, A. M., & Czerny, B. 2005, *arXiv e-prints*, astro. <https://arxiv.org/abs/astro-ph/0512310>
- Sadaula, D. R., Bautista, M. A., García, J. A., & Kallman, T. R. 2023, *ApJ*, 946, 93, doi: [10.3847/1538-4357/acbd40](https://doi.org/10.3847/1538-4357/acbd40)
- Sadaula, D. R., & Kallman, T. R. 2024, *ApJ*, 960, 120, doi: [10.3847/1538-4357/ad0553](https://doi.org/10.3847/1538-4357/ad0553)
- Silk, J., & Rees, M. J. 1998, *A&A*, 331, L1, doi: [10.48550/arXiv.astro-ph/9801013](https://doi.org/10.48550/arXiv.astro-ph/9801013)
- Silva, C. V., Uttley, P., & Costantini, E. 2016, *A&A*, 596, A79, doi: [10.1051/0004-6361/201628555](https://doi.org/10.1051/0004-6361/201628555)
- Tarter, C. B., Tucker, W. H., & Salpeter, E. E. 1969, *ApJ*, 156, 943, doi: [10.1086/150026](https://doi.org/10.1086/150026)
- Tombesi, F., Cappi, M., Reeves, J. N., et al. 2010, *A&A*, 521, A57, doi: [10.1051/0004-6361/200913440](https://doi.org/10.1051/0004-6361/200913440)